ENGINEERING

Carbon nanotube supported oriented metal organic framework membrane for effective ethylene/ethane separation

Ruicong Wei[1]†, Xiaowei Liu[1]†, Zongyao Zhou[1], Cailing Chen[1], Youyou Yuan[2], Zhen Li[1], Xiang Li[1], Xinglong Dong[1], Dongwei Lu[1], Yu Han[1], Zhiping Lai[1]*

Copyright © 2022 The Authors, some rights reserved; exclusive licensee American Association for the Advancement of Science. No claim to original U.S. Government Works. Distributed under a Creative Commons Attribution NonCommercial License 4.0 (CC BY-NC).

Zeolitic imidazolate framework 8 (ZIF-8) is effective for C_3H_6/C_3H_8 separation because of the "sieving effect" of a six-membered (6-M) window. Here, we demonstrate that ZIF-8 is a versatile material that could effectively separate C_2H_4 from C_2H_6 via its 4-M window along the <100> direction. We established a facile and environmentally friendly carbon nanotube (CNT)–induced oriented membrane (CNT-OM) approach to fabricate a {100}-oriented ZIF-8 membrane (100-M). In this approach, 2-methyimidazole was anchored onto the CNT surface followed by 3-hour in situ growth in aqueous solution at room temperature. The obtained 100-M, whose 4-M window is aligned along the transport pathway, showed ~3 times higher C_2H_4/C_2H_6 selectivity than a randomly oriented membrane. Thus, this work demonstrates that the membrane orientation plays an important role in tuning selectivity toward different gas pairs. Furthermore, 100-M exhibited excellent mechanical stability that could sustain the separation performance after bending at a curvature of ~109 m^{-1}.

INTRODUCTION

Metal organic frameworks (MOFs), a type of microporous polycrystalline materials, have drawn research attention owing to its high porosity, tunable structural and chemical properties, and ease of synthesis (*1*, *2*). MOFs have one or multiple channels in different crystallographic orientations. In general, each crystallographic orientation has a specific window aperture. The window aperture functions to discriminate the molecules with diameters beyond the aperture size. MOFs generally have the window aperture at the gas molecule scale, making them good candidates to be fabricated into membranes for gas separations. Most of the reported polycrystalline MOF membranes are composed of crystals with random orientations. However, oriented polycrystalline MOF membranes are more desirable as they could potentially not only minimize the grain boundary defects but also regulate gas separation performance by tuning the crystallographic orientation relative to the substrate (*3*–*6*).

Zeolitic imidazolate framework 8 (ZIF-8) has a six-membered (6-M) window and a 4-M window along directions of <111> and <100>, respectively. ZIF-8 membrane has been demonstrated to be exceptionally effective to separate propylene (C_3H_6) from propane (C_3H_8) (*7*–*10*). This effectiveness is due to the "swing effects" of 2-methyimidazole (2-MIM) of the 6-M window that could enlarge the aperture from 3.4 to 5.2 Å (*11*, *12*). As a result, propylene (critical diameter, ~4.0 Å) and propane (critical diameter, ~4.2 Å) could pass through the window with a hugely different diffusion rate, enabling an unexpected high C_3H_6/C_3H_8 selectivity (*11*). In contrast, the 4-M window along the <100> direction was used to be thought disadvantageous in gas separations owing to its extremely small aperture (<3 Å) (*13*), which, in theory, could only allow He (diameter, ~2.66 Å) and H_2 (diameter, ~2.9 Å) to pass through. However, simulation studies suggested that the window aperture could be enlarged to above 4.0 Å (*14*) via swing effects, which means that C_2H_4 and C_2H_6 could potentially pass through the window and achieve a diffusion selectivity along <100>. This piqued our enthusiasm to synthesize a {100}-oriented ZIF-8 membrane to test its potential in C_2H_4/C_2H_6 separation performance.

Fabrication of oriented MOF films/membranes is always challenging. Seeding and secondary growth is the most popular approach used in synthesis of oriented membranes. Two general growth mechanisms were observed in this approach. One mechanism is similar to epitaxy growth through which an oriented seed layer forms first followed by a secondary growth during which the membrane grows along the seed layer orientation. Oriented membranes composed of ZIF-69 (*15*), MOF-5 (*16*), UiO-66 (*17*, *18*), and MIL-125 (*4*) were formed following this mechanism. The other mechanism was evolutionary growth (*19*, *20*) in which the fast growth direction will dominate the out-plane membrane orientation via competitive crystal growth. Oriented membranes of materials such as UiO-66 (*18*, *21*) and ZIF-8 (*22*) were proposed to be generated following this mechanism. Beside seeding and secondary growth, another approach for oriented–MOF film/membrane synthesis is layer-by-layer (LbL) growth in which the substrate was functionalized with a self-assembled monolayer (SAM). The SAM normally has head groups such as —NH_2, —OH, and —COOH that could form a coordinate bond with metal ions of a specific MOF. The LbL growth is conducted by immersing the functionalized substrate alternatively into the metal ions and ligand solutions (*23*). Using this approach, a {110}-oriented ZIF-8 membrane has been obtained by functionalizing the substrate with a layer of SAM with —OH head groups followed by LbL growth for ~300 cycles (*24*). Nevertheless, while the LbL approach is a welcome approach for oriented–MOF film formation, it is very difficult to result in a good-quality membrane for gas separation applications. Probably because of the nonuniform SAMs, the resultant membrane always suffers from a large amount of defects that requires multiple steps of substrate treatment and hundreds of

[1]Chemical Engineering Program, Division of Physical Science and Engineering, King Abdullah University of Science and Technology (KAUST), Thuwal 23955-6900, Saudi Arabia. [2]Core Labs, King Abdullah University of Science and Technology (KAUST), Thuwal 23955-6900, Saudi Arabia.
*Corresponding author. Email: zhiping.lai@kaust.edu.sa
†These authors contributed equally to this work.

crystal growth cycles to heal (*25*), making it not a preferable approach for membrane fabrication. However, anchoring the chemical node (e.g., metal ion) of a crystalline framework is a brilliant idea for oriented-membrane growth owing to its potential to induce uniform nucleation on the substrate. Inspired by this idea, we made the thought at a different angle: Instead of anchoring metal ions, the ligand could also be anchored to induce an oriented membrane. A substrate that intrinsically has a uniform distribution of coordination sites would be an ideal choice to avoid multiple steps of surface functionalization.

After a careful literature study, we selected carbon nanotube (CNT) to be the candidate to anchor the ligand 2-MIM as shown in Fig. 1A. As previous reported (*26*), the NH groups of 2-MIM could create a regional positive charge when attached to CNT, which induces a regional negative charge of π bond on the CNT surface. As a result, 2-MIM could be anchored onto the CNT surface via a strong electrostatic attraction. There might be a further negative charge transfer from the π bond of the aromatic group to 2-MIM (*27*), which could potentially strengthen the bond between 2-MIM and CNT (see fig. S1). The intrinsic homogeneous distribution of aromatic π—π bond on CNT ensures uniform crystal nucleation, which could potentially lead to an oriented membrane with low defect density. Beside its possibility in inducing an oriented membrane elaborated above, CNT has high mechanical strength, which could potentially help improve the strength of the membrane if a CNT-membrane matrix was formed.

We then decided to synthesize the membrane in an aqueous solution that could trigger rapid ZIF-8 nucleation and crystal growth (*28*), suppressing secondary nucleation and nonuniform crystal growth. The fast nucleation could quickly consume the reactants, resulting in a low-supersaturation precursor solution, favoring the crystal competition growth along <100> in ZIF-8 (*29*). In addition, conducting synthesis in an aqueous solution could also enable an environmentally friendly route for membrane fabrication.

As a proof of concept, in this work, we developed a CNT-induced oriented membrane (CNT-OM) approach. In this approach, we fabricated a thin layer of single-walled CNT support via vacuum filtration of the CNT aqueous solution onto an anodized alumina (AAO) to form a CNT-AAO substrate. The CNT layer has ~152-nm thickness (fig. S2A) with a root mean square roughness of ~10.1 nm (fig. S2, B and C). The CNT-AAO substrate was immersed into the 2-MIM aqueous solution for ~3 min at room temperature to allow

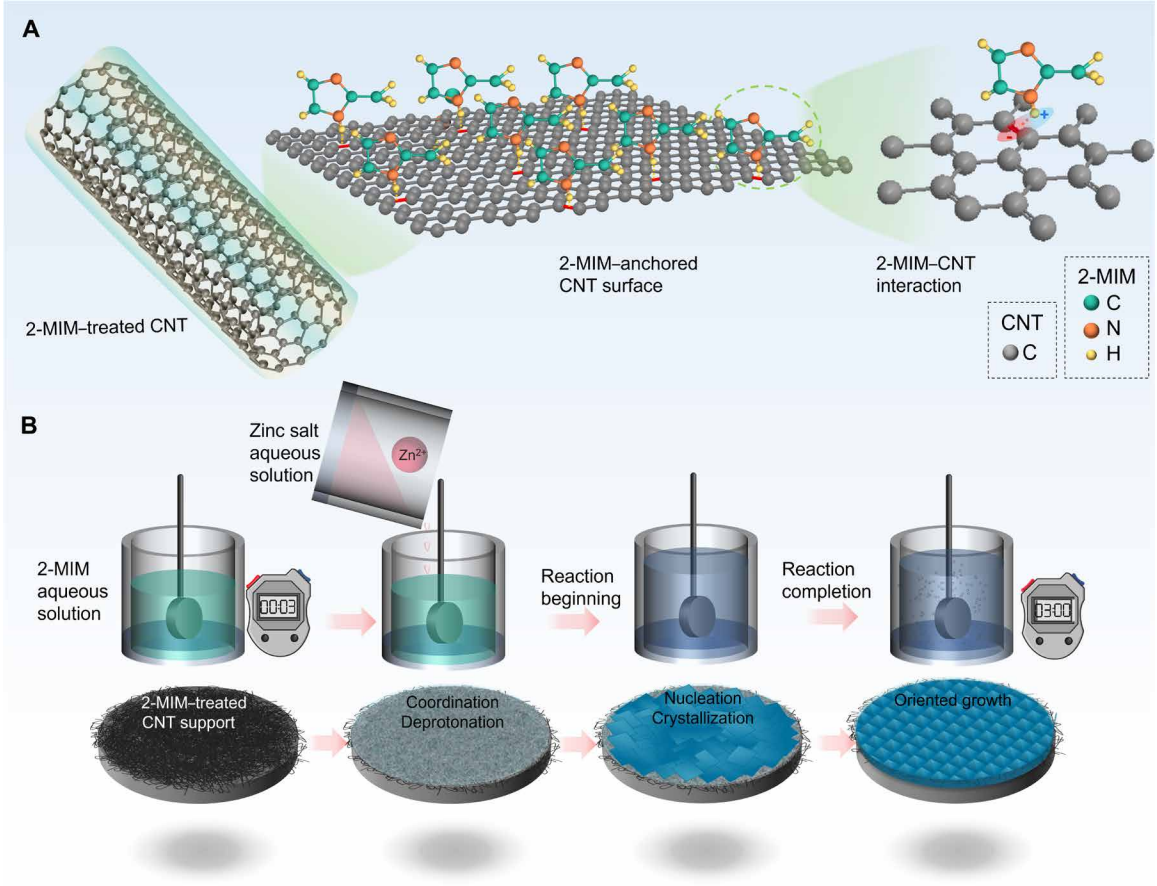

Fig. 1. Schematic illustration of synthesis strategy using 2-MIM–anchored CNT as the support to direct {100}-oriented ZIF-8 membrane. (**A**) The left image shows an overview of 2-MIM–treated CNT. The middle image gives a snapshot of a small area of 2-MIM–anchored CNT surface. The right image shows the interaction between π bond of CNT and NH groups bond of 2-MIM via opposite charge attraction. (**B**) Schematic illustration of the synthesis procedure of {100}-oriented ZIF-8 membrane. At the beginning, the CNT-supported AAO substrate was immersed into the 2-MIM aqueous solution for 3 min to anchor 2-MIM onto the CNT support. After that, the zinc ion solution was added into the 2-MIM solution to start the reaction. The reaction followed coordination/deprotonation, nucleation, crystallization, and oriented-membrane growth. After 3 hours, the oriented membrane was formed.

2-MIM to be anchored onto the CNT surface (Fig. 1B). To verify this, the 2-MIM–treated CNT was investigated by Fourier-transform infrared (FTIR) spectroscopy (fig. S3), Raman spectroscopy (fig. S4), and x-ray photoelectron spectroscopy (XPS; fig. S5) in comparison with pristine CNT and pure 2-MIM. The results of the three measurements were nicely converged to confirm that the 2-MIM was successfully anchored onto the CNT surface after the treatment (Fig. 1B). Zinc ion aqueous solution was then poured into the 2-MIM solution to allow the reaction to start in the same condition. During this process, the reaction underwent coordination (fig. S1), deprotonation, crystal nucleation, and growth. After 3 hours, a {100}-oriented ZIF-8 membrane was obtained. We then did permeation test on this membrane in gas pairs of C_2H_4/C_2H_6, C_3H_6/C_3H_8, and $C_4H_{10}/isoC_4H_{10}$. The membrane showed superior C_2H_4/C_2H_6 separation performance that placed way beyond the upper bond up to today. Moreover, this membrane exhibited astonishingly high mechanical strength and could sustain the separation performance after 109 m^{-1} bending curvature, which is a highly desirable attribute in terms of industrial application considering that inorganic polycrystalline membranes always suffer from fragility and brittleness.

RESULTS

The evolution of membrane growth upon time was illustrated in Fig. 2 (A to G) by scanning electron microscope (SEM) images and x-ray diffraction (XRD) patterns (see fig. S6 for XRD configurations). At 5 min, the CNT layer has been filled with densely packed "cement" (Fig. 2A), which was confirmed by XRD to be (110)-dominated ZIF-8 (5 min; Fig. 2G). At 10 min, the cement-filled CNT surface has been fully covered with a layer of loosely packed ZIF-8 crystals (Fig. 2B) with rhombic dodecahedron morphology (Fig. 2H). In particular, most of the crystals have their (110) face exposed upward (highlighted in the dashed red circles). At 30 min (Fig. 2C), the crystal layer grew in a more packed manner and was composed of mixed {110}-oriented crystals (red dashed circles) and occasionally {100}-oriented crystals (blue dashed circles). From 30 to 120 min, {100}-oriented crystals were increasingly formed compared with that of {110} (Fig. 2, C to E). The associated XRD patterns (30, 60, and 120 min; Fig. 2G) also show that (200) reflection was becoming progressively dominant. At 180 min, a ZIF-8 membrane (Fig. 2F) with densely intergrown {100}-oriented crystals (Fig. 2H) were formed. The XRD pattern (180 min; Fig. 2G) also shows that (200) reflection became the most dominant with other reflections visually diminished. The degree of membrane orientation was analyzed by crystallographic preferred orientation (CPO) index (table S1). The $CPO_{200/110}$ and $CPO_{200/211}$ were 115.6 and 81.8, respectively, which were much higher than the corresponding values of a Ran-M ($CPO_{200/110}$ = 2.9; $CPO_{200/110}$ = 1.6). The oriented membrane was further analyzed by two-dimensional (2D) XRD and pole figure XRD. 2D XRD image (Fig. 2I) shows that the (200) plane exhibits the highest brightness with a slightly visible (110) plane. The pole figure map (Fig. 2J), conducted at fixed θ of 5.2° corresponding (200) plane, shows there two purple dots (high intensity) at the center with other parts of the map uniformly filled with pink color (low intensity). Combing all the XRD studies of different configurations and CPO index, we can confirm that the highly {100} out-of-plane oriented ZIF-8 membrane has been obtained within 3 hours of synthesis at room temperature. To verify that it is the 2-MIM–anchored CNT layer that dictates such an oriented membrane formation, we also did three comparison experiments as discussed in the following.

We did the first comparison experiment to grow a ZIF-8 membrane on a dopamine-treated AAO using the identical synthesis conditions of {100}-oriented membrane (100-M). This experiment was to delineate the effects of dopamine on crystal growth as the AAO that we used in this research was pretreated with dopamine to make sure the CNT attach firmly onto the support without peeling off. The results showed that instead of a membrane, a layer of randomly oriented discrete ZIF-8 crystals was formed (fig. S7). The second experiment was conducted by treating the CNT with zinc ion solution for 3 min, instead of 2-MIM, before mixing the two solutions to start the reaction. The rest of the synthesis conditions were kept the same. This experiment was to demonstrate that it is 2-MIM rather than zinc ion that dictates uniform nucleation at the CNT surface. The resultant membrane was randomly oriented and composed of loosely packed ZIF-8 crystals (fig. S8). The third experiment was conducted by mixing 2-MIM and zinc ion solution first followed by immersing the pristine CNT-supported AAO substrate to grow the membrane. The synthesis condition was kept the same besides the 3-min 2-MIM pretreatment. This experiment was performed to demonstrate the key effect of the 2-MIM anchoring procedure for the 100-M growth. The resultant pristine CNT-supported membrane was randomly oriented (fig. S9). Combined the results of the three comparison experiments, we confirmed that the 2-MIM–anchored CNT dictates the formation of {100}-oriented ZIF-8 membrane. We further investigated the effects of outer diameters (fig. S10) and thickness of CNT (fig. S11) on the {100} orientation formation. The resultant membranes all showed dominant {100} orientations based on combined XRD and SEM imaging characterizations (figs. S12 and S13). These results imply that it is the intrinsic chemical structure rather than the physical size or layer thickness of CNT that facilitates the formation of {100} orientation.

The lattice structure of 100-M was studied by high-resolution transmission electron microscopy (HRTEM). The HRTEM image together with selected-area electron diffraction (SAED) pattern (Fig. 3A) further confirmed the well-aligned {100} orientation. The CTF-corrected HRTEM (Fig. 3B) shows a reverse-engineered image of {100} plane with examples of 4-M window highlighted in red squares. The average aperture of this window based on this image was statistically determined to be ~2.5 Å. The window was composed of four tetrahedrally coordinated zinc ions connected by four 2-MIM molecules (Fig. 3C, highlighted in red squares). The actual window aperture is dictated by the orientation of the four 2-MIM molecules (Fig. 3D, highlighted in red dashed circles). If the 2-MIM molecules rotated to the position at which C—CH_3 bonds are perpendicular to the {100} plane (Fig. 3E), then 4-M window aperture could be enlarged to above 4.0 Å, allowing larger gas molecules with size beyond the original aperture to pass through for a potential diffusive separation. This kind of window-opening process has been proved possible by combing adsorption studies and molecule simulation (*13*, *14*). Beside the window size, the gas separation performance could also be potentially enhanced by a tightened intergrown {100}-oriented crystals. This will lead to a membrane with lower grain boundary defects (*4*–*6*). To give a glimpse of this potential effects, we investigated the chemical bonds of 100-M via FTIR spectroscopy (Fig. 3F) in comparison with a randomly oriented membrane (Ran-M; fig. S9). The two patterns show almost identical features with only one peak shift of 100-M toward a lower wave number at 1418 cm^{-1}. This peak

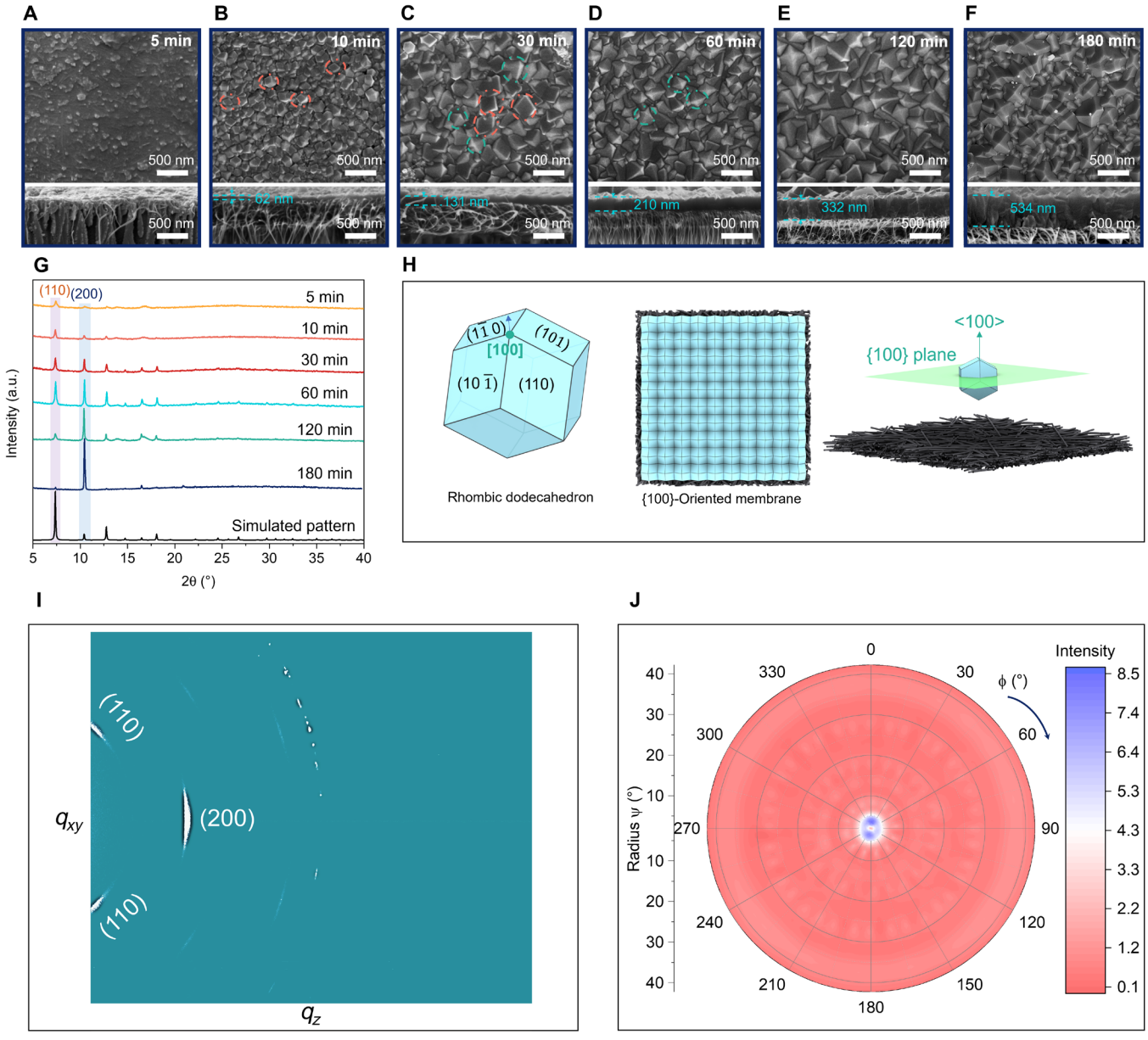

Fig. 2. SEM and XRD characterizations of {100}-oriented ZIF-8 membrane. SEM images of ZIF-8 membrane growth after (**A**) 5 min, (**B**) 10 min, (**C**) 30 min, (**D**) 60 min, (**E**) 120 min, and (**F**) 180 min. (**G**) Time series of XRD patterns of ZIF-8 membrane growth from 5 to 180 min as compared with the simulated pattern. a.u., arbitrary units. (**H**) Schematic illustration of a ZIF-8 crystal with rhombic dodecahedron morphology, 100-M and {100} plane parallel to the CNT-AAO substrate. The rhombic dodecahedron shown at the left consists 12 rhombic faces belonging to the <110> family. The four labeled (110), (10$\bar{1}$), (1$\bar{1}$0), and (101) faces intercept at the [100] direction. (**I**) Two-dimensional XRD image of 100-M. (**J**) Pole figure XRD map of 100-M with ϕ rotation from 0° to 360° and radius Ψ tiled from 0° to 40°.

was assigned to C—H bending of the imidazole ring (*30*), suggesting that the 2-MIM in 100-M was less perturbed compared with Ran-M. This observation may be due to the result that the oriented membrane has crystals aligned well with each other, leading to less grain boundary defects, thus less associated chemical bond distortions. This result underlined the potential advantage of 100-M for good separation performances.

To investigate the potential of 100-M in gas separation applications, we first did permeation tests of binary gas C_2H_4/C_2H_6, C_3H_6/C_3H_8, and $C_4H_{10}/isoC_4H_{10}$ (see table S2 for gas molecule sizes). The test was conducted at room temperature and 1 bar using the Wicke-Kallenbach technique (fig. S14). The results (fig. S15 and table S3) show that the gas permeances decreased with increased molecular size from C_2H_4 to C_3H_8. The permeances of C_3H_8 and nC_4H_{10} were similar and both below 1 gas permeance unit (GPU), while we did not detect any $isoC_4H_{10}$ (diameter, 5.0 Å) under the test conditions used in this study. These results suggest that the cutoff size for this 100-M is between C_3H_6 (4.0 Å) and C_3H_8 (4.2 Å), which is close to the fully opened 4-M window aperture. This nice correlation also implies that the 100-M had low defect density, further highlighting the advantage of oriented membrane.

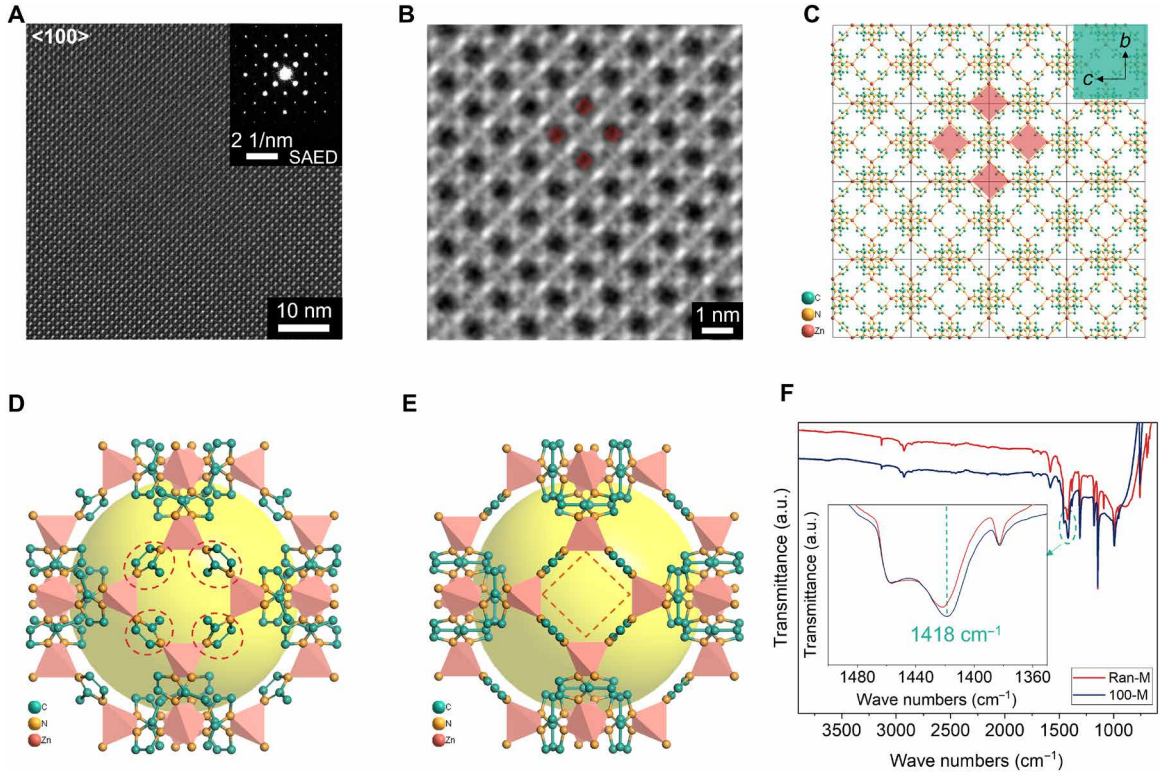

Fig. 3. 4-M window size and structure characterizations for {100}-oriented ZIF-8 membrane. (**A**) HRTEM image viewing along the <100> direction of 100-M with an inserted SAED pattern. (**B**) CTF-corrected HRTEM showing the 4-M window at the {100} plane with examples of the window highlighted in red squares. (**C**) Schematic illustration of {100} plane composed of 4 × 4 cells with examples of 4-M window highlighted in red squares. (**D**) Schematic illustration of 4-M window of a unit cell of ZIF-8 with the 2-MIM components within the window highlighted in red dashed circles. (**E**) Schematic illustration of "opened" 4-M window of a unit cell of ZIF-8 with the 2-MIM rotated to the position perpendicular to the {100} plane. (**F**) An overview of FTIR spectra of 100-M compared with Ran-M with an inserted spectra showing the peak shift of 100-M at 1418 cm^{-1}.

The separation performances of 100-M for C_3H_6/C_3H_8 and C_2H_4/C_2H_6 were compared with those of Ran-M (tables S3 and S4). With a similar thickness (Fig. 2F and fig. S9D), 100-M had both lower C_3H_6 permeance (~18.1 GPU) and C_3H_6/C_3H_8 selectivity (~40) than those of Ran-M (C_3H_6 permeance, ~53.4 GPU; C_3H_6/C_3H_8 selectivity, ~153). In contrast, for C_2H_4/C_2H_6 separation, 100-M had an impressive C_2H_4/C_2H_6 selectivity of ~9.6 with a C_2H_4 permeance of ~244 GPU (Fig. 4A, fig. S16A, and table S3). This selectivity is ~3 times higher than that of Ran-M (selectivity, ~3.4; C_2H_4 permeance, ~581 GPU). The poorer performance of 100-M in C_3H_6/C_3H_8 separation and superior performance in C_2H_4/C_2H_6 separation, as compared with Ran-M, were mainly attributed to the narrower 4-M window aperture along <100> (Fig. 3, A to E). The online stability test for 100-M showed that it could keep the C_2H_4/C_2H_6 separation performance with little changes for ~200 hours (Fig. 4B and fig. S16B), proving the high stability of this membrane.

The membrane was further tested by varying the molar feed ratios of C_2H_4 and C_2H_6 (C_2H_4:C_2H_6) at 1 bar and room temperature. The results (Fig. 4C) show that both C_2H_4 permeance and C_2H_4/C_2H_6 selectivity decreased while C_2H_6 permeance slightly increased with increased feed ratio. This phenomenon could be explained by the pressure effect that for both C_2H_4 and C_2H_6, an increase in partial pressure comes with a decreased permeance but an increased flux (fig. S16C) and vice versa (*31*). The effects of pressure on C_2H_4/C_2H_6 gas separation were further investigated by increasing the feed pressure from 1 to 8.5 bar while kept the feed ratio at 50:50 (Fig. 4D). Similarly, permeance of both C_2H_4 and C_2H_6 decreased with increased pressure. In particular, C_2H_4 permeance decreased steeply from 1 to 3 bar and kept at a similar slope with that of C_2H_6 from 3 bar onward. Consequently, C_2H_4/C_2H_6 selectivity sharply dropped from 1 to 3 bar and kept relatively constant at ~7.5 from 3 to 8.5 bar. The increased pressure also resulted in a substantially enhanced C_2H_4 flux (fig. S16D). These results demonstrate that 100-M can sustain a good separation performance at relatively high pressures, which is a good attribute for potential industrial applications. 100-M also had good mechanical strength and could sustain the gas separation with little changes after bending the membrane to the curvature of ~109 m^{-1} (fig. S17A). This impressive strength is mainly contributed by the intrinsic high mechanical strength of CNT that improves the bending strength for both AAO and ZIF-8. On the one hand, the AAO bending strength was improved through which the CNT layer absorbed and redistributed the applied force at the porous side of AAO. As a result, the extent of localized plastic deformation and layered ruptures of AAO was reduced (*32*), leading to a significantly improved bending strength compared with that of pristine AAO (fig. S17B). On the other hand, the CNT has been partially embedded with the ZIF-8 membrane (Fig. 2A), reinforcing the bending strength of ZIF-8 (*33*).

Beside mechanical stability, we also investigated the thermal stability of 100-M from 20° to 60°C (Fig. 4E and fig. S16E). Both C_2H_4

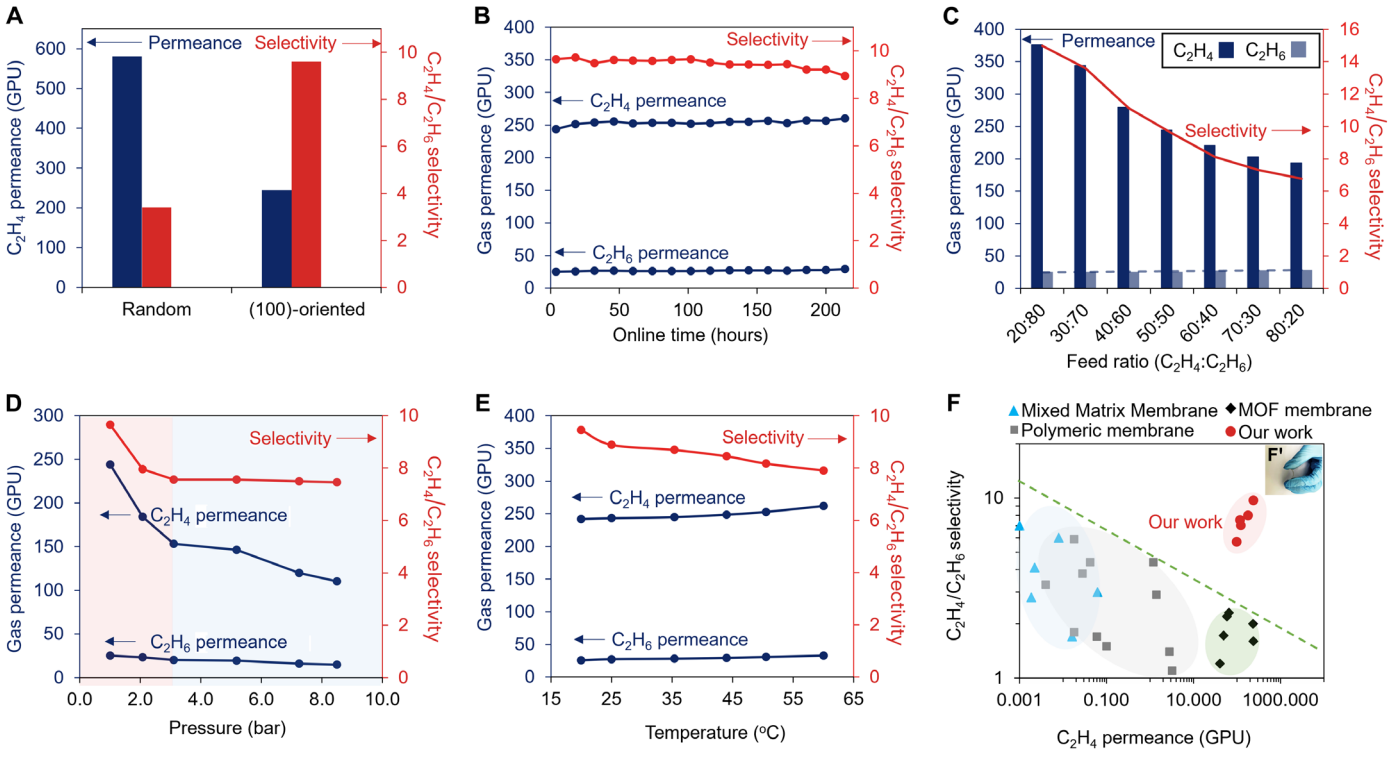

Fig. 4. Gas separation performances of 100-M. (**A**) C_2H_4/C_2H_6 separation performance of 100-M compared with Ran-M. (**B**) Long-term stability of 100-M for C_2H_4/C_2H_6 separation at room temperature and 1 bar. (**C**) C_2H_4/C_2H_6 separation performance of 100-M at different feed ratios. (**D**) C_2H_4/C_2H_6 separation performances of 100-M as a function of feed pressure. (**E**) C_2H_4/C_2H_6 separation performances of 100-M as a function of temperature. (**F**) C_2H_4/C_2H_6 separation performances of 100-M compared with other reported membranes after bending at a curvature of 109 m^{-1} shown in the inserted image F′. Because less than ~5% of separation performance changes were observed before and after bending, we used the data after bending for the comparison. MMM, mixed matrix membrane.

and C_2H_6 permeances increased, while the C_2H_4/C_2H_6 selectivity slightly decreased with the increased temperature. This phenomenon could be due to the decreased affinity of both C_2H_4 and C_2H_6 on the intersurface of ZIF-8 channel with the increased temperature. At the same time, C_2H_6 had higher extent of affinity decline compared with that of C_2H_4. Nevertheless, the results still show that 100-M could maintain a good separation performance under elevated temperatures. We lastly compared our results with other reported membranes in C_2H_4/C_2H_6 separation as plotted in Fig. 4F with the upper bound (green dashed line) drawn according to (*34*). The separation performances of this work, no matter before or after bending (Fig. 4F′), all sit beyond the upper bound, demonstrating the outstanding performance of 100-M.

To further confirm the functionality of 4-M window at the {100} plane in C_2H_4/C_2H_6 separation, we conducted molecular dynamics (MD) to simulate the membrane process of C_2H_4/C_2H_6 separation across the <100> direction (fig. S18 and movie S1). Because the membrane thickness in the simulation was only equivalent to four unit cells, we converted the gas permeance into permeability to do a direct comparison with the experimental data. The simulation results gave a C_2H_4 permeability of 113 barrer and a C_2H_4/C_2H_6 selectivity of ~11, which is very close to our experimental data (C_2H_4 permeability, 130.3 barrer; C_2H_4/C_2H_6 selectivity, 9.6). The agreement between the simulation and experiment results confirmed the viability of 100-M for C_2H_4/C_2H_6 separation.

DISCUSSION

One of the key findings of this work is to demonstrate that the 2-MIM–anchored CNT dictates the 100-M formation. This finding has been verified by the three comparison experiments (figs. S7 to S9). The study of the membrane evolution formation indicated that {110}-oriented cement CNT-ZIF-8 composite (Fig. 2A) triggered a nonperfect {110}-oriented membrane formation at early stages (Fig. 2B). Then, the membrane gradually transformed into {100} orientation as the reaction proceeded to the later stages. This observation disagrees with the epitaxy growth mechanism in which the crystal growth in the secondary layer normally follows the orientation of the first layer by lattice matching (*25*). In contrast, the growth phenomenon observed in this work, at first glance, seemed to follow the evolutionary growth mechanism (*19*, *20*). In this mechanism, despite the crystal orientation at the early stage, the fastest growth direction will dominate the out-of-plane membrane orientation via competitive crystal growth as the reaction proceeds to equilibrium at later stages. This mechanism was proved to form *c*-oriented MFI zeolite films obtained via the seeding and secondary growth method (*35*). For the case of ZIF-8, Caro *et al.* (*22*) obtained a 100-M via the seeding and secondary growth approach and proposed that the oriented growth may be explained by the evolutionary growth mechanism. In their work, the seed layer was dip-coated onto an alumina support followed by a secondary growth at 100°C using methanol and sodium formate as the solvent and the modulator, respectively.

However, the CNT-OM approach reported in this work was completely incomparable with the work reported by Caro *et al.* (*22*). On one hand, the seed layer was randomly oriented in their work, while we did not conduct any seeding process in our work. On the other hand, the precursor solution and reaction conditions are completely different, which means that membrane formation in our work may follow a different crystal growth path considering that the synthesis parameters significantly affect the crystal growth habit in MOF synthesis (*36*).

Taking another look at the in situ crystal growth transformation from {110} to {100} observed in our work (Fig. 2, A to G), instead of evolutionary growth mechanism (*19*, *20*), we rather believe that 100-M formation may resemble a ZIF-8 single-crystal transformation growth (*29*). This transformation growth is mainly governed by precursor supersaturation condition (concentration of Zn^{2+} and 2-MIM). At the early stage, the crystal favored to grow along the {110} direction at high supersaturation condition. As the reaction proceeded, the supersaturation condition became lower as more Zn^{2+} and 2-MIM were consumed, resulting in a preferrable growth along the <100> direction. This change of crystal growth habit could be due to the fact that the precursor species/intermediates formed at later stages are more energetically favorable to attach along the <100> direction compared with other directions (*29*, *37*). The preferred growth along <100> propagated toward both perpendicular and parallel directions relative to the substrate, resulting in 100-M. Although we believe that this is the most reasonable explanation based on the available experiment data so far, more research efforts needed to be conducted to fully understand the crystal orientation transformation observed in this work.

Another interesting finding of this work is the improved C_2H_4/C_2H_6 separation performance of 100-M compared with its random counterpart. Both 100-M (Fig. 2F) and Ran-M (fig. S9C) were composed of intergrown rhombic dodecahedral crystals with 12 exposed (110) faces (Fig. 2H), suggesting that gas molecules always need to enter the membrane through the 6-M window in the {110} plane despite the membrane orientations. However, the gas permeation test showed that 100-M exhibited much lower permeances of both C_2H_4 and C_3H_6 (Fig. 4A and table S4), implying that the 4-M window aligning with {100} orientation reduced the molecule flux because of its narrower aperture than that of 6-M window. Thus, we deduced that 4-M window acts as a "bottleneck" along with <100> direction to form a dominant gas transport path. As a result, the smaller molecules (e.g., C_2H_4 and C_2H_6) could achieve significantly improved gas selectivity.

In conclusion, we established a facile and environmentally friendly CNT-OM approach. In this approach, 2-MIM was anchored onto CNT surface via a 3-min direct immersion treatment followed by 3 hours of in situ growth at room temperature in an aqueous solution. The 2-MIM–anchored CNT functions to ensure both uniform nucleation and oriented growth. The {100}-oriented ZIF-8 membrane was proved to be unexpectedly effective in C_2H_4/C_2H_6 separation, which has a selectivity up to ~3 times higher than a randomly oriented membrane. To our best knowledge, this is the first report to demonstrate that membrane orientation can tune separation selectivity toward different gas pairs. The outstanding C_2H_4/C_2H_6 separation performance was confirmed to be due to the narrow aperture of 4-M window along the <100> direction by combing experiment and simulation results. The resultant 100-M also showed excellent thermal and mechanical stability that could sustain the separation performances after a bending at curvature of 109 m^{-1}.

This work reports the first oriented polycrystalline membrane fabricated by in situ growth and opens more possibilities to explore CNT-supported MOF membranes in directing both oriented growth and mechanical strength improvement. We also highlighted the great potential of alter separation performances via tuning crystal orientations, promoting more research opportunities to extend MOF membrane's capacity in various gas separations. We envisioned the challenges in using large commercial substrates for synthesis of oriented membranes, which still requires substantial further research efforts in the foreseeable future.

MATERIALS AND METHODS

Chemicals and materials

Zinc acetate dihydrate [$Zn(CH_3COO)_2{\cdot}2H_2O$, > 99%; Sigma-Aldrich], 2-MIM ($CH_3C_3H_2N_2H$, 99%; Acros Organics), sodium dodecylbenzene sulfonate [$CH_3(CH_2)_{11}C_6H_4SO_3Na$, 98%; Aladdin], dopamine hydrochloride [$(HO)_2C_6H_3CH_2CH_2NH_2{\cdot}HCl$, 98%; Sigma-Aldrich], and potassium chloride (KCl, > 99%; Sigma-Aldrich) were all used as received unless otherwise stated. Deionized water (DI water) was obtained using a Milli-Q Academic ultrapure water system. CNTs (single-walled, diameter <2 nm, length 5 to 30 μm, >95%) powder was purchased from XFNANO, China. tris(hydroxymethyl)aminomethane hydrochloride [tris-HCl, $NH_2C(CH_2OH)_3{\cdot}HCl$, 10 mM, pH 8.5] buffer was bought from Sigma-Aldrich. Anodic aluminum oxide substrates (AAO; diameter 25 mm, pore size 0.02 μm, thickness 60 μm) were gained from Whatman.

Preparation of the CNT solution and the CNT-AAO support

Followed our previously reported procedure (*38*), CNT powder (100 mg) and sodium dodecylbenzene sulfonate (1 g) were sonicated in DI water (1 liter) for 1.5 hours. The mixture was centrifuged (15,000 rpm) for 40 min to remove any undispersed CNT powder. The collected supernatant was collected for further usage. AAO substrates were immersed in a dopamine solution (2 mg/ml) at 10 mM tris-HCl buffer (pH 8.5) for 1 hour at room temperature under 60-rpm shaking for the preparation of dopamine-treated AAO substrates. The CNT solution was filtered under vacuum onto the dopamine-treated AAO substrates. The thickness of the CNT layer can be controlled by the amount of CNT solution used. Then, the prepared CNT-AAO substrates were dried for 15 min in a vacuum oven at 60°C. After that, the CNT-AAO substrates were washed by DI water to thoroughly remove sodium dodecyl-benzenesulfonate.

Preparation of precursor solutions for fabrication of ZIF-8 membranes

2-MIM solution was prepared by dissolving 4.105 g of 2-MIM in 50 ml of DI water. Zinc ion solution was prepared by dissolving 0.183 g of Zn $(CH_3COO)_2{\cdot}2H_2O$ in 10 ml of DI water.

In situ growth of {100}-oriented ZIF-8 membranes on CNT-AAO substrate

The CNT-AAO substrate was first immersed into the 2-MIM solution for 3 min, and afterward, the zinc precursor solution was poured into the 2-MIM solution. The reaction was carried out at room temperature and ambient pressure for 3 hours. The resultant ZIF-8 membrane was then thoroughly washed by DI water followed by methanol and lastly activated in methanol for gas permeation tests.

Mixed-gas permeation test

The Wicke-Kallenbach technique, as described in fig. S14, was used to perform the permeation tests in this work. At the feed side, a total flow of 50 cm^3 min^{-1} of equimolar gas mixtures, such as C_2H_4/C_2H_6, C_3H_6/C_3H_8, or $nC_4H_{10}/isoC_4H_{10}$, was introduced into the permeation cell, while at the permeate side, the sweep gas (Ar) was applied with a flow rate of 50 cm^3 min^{-1}. The feed side pressure was manipulated from 1 to 8.5 bar according to the test conditions, while the permeate side pressure was always maintained at atmosphere pressure. The composition of the permeate streams was online determined by a gas chromatograph (Agilent 7890A) equipped with a flame ionization detector.

The permeance of the membranes is calculated as

$$F_i = \frac{J_i}{A \times \Delta P_i} \quad (1)$$

where J_i is the flux of the component i (mol/s), A is the effective area of the membrane (m^2), and ΔP_i is the partial pressure drop across the membrane of the component i.

The permeability, an intrinsic property of the membrane material, is computed as

$$P_i = F_i \times l \quad (2)$$

where l is the thickness of the membrane.

The ideal selectivity for membrane separation is then defined as

$$S_{i,j} = \frac{F_i}{F_j} = \frac{P_i}{P_j} \quad (3)$$

where F and P refer to the single-component permeances and permeabilities of the competing gases i and j, respectively.

For real binary mixtures, the separation factor could be calculated as

$$a_{i,j} = \frac{y_i/y_j}{x_i/x_j} \quad (4)$$

where x and y are the molar fractions of the corresponding component in the feed and permeate stream, respectively.

Material characterization

SEM images were taken by a FEI Magellan 400L XHR SEM at an acceleration voltage of 3 kV to observe the morphology of the membrane samples. The samples were prepared by sputter coating with Pt/Pd for 12 s at 20 mA. Atomic force microscope (AFM) images were obtained from a Bruker Dimension Icon AFM to analyze the surface roughness and 3D height of the membranes. XRD patterns were recorded on a Bruker D8 ADVANCE Twin X-ray diffractometer (40 kV, 40 mA) with Cu Kα radiation and a scanning step size of 0.0085° 2θ, while 2D and the pole figure XRD patterns were collected on a Bruker D8 Eiger diffractometer (Cu Kα, 40 kV, 40 mA). FTIR spectroscopy was conducted on a Thermo Scientific Nicolet iS10 instrument to characterize the chemical properties of the samples. The attenuated total reflection mode was used with a diamond window. Sixty-four scans were used for per measurement at a resolution of 0.964 cm^{-1}, and the samples were dried under a dynamic vacuum at 60°C overnight before measurement. XPS was carried out using a Kratos AXIS Ultra DLD system equipped with a monochromatic x-ray source and a dual Al-Mg anode. A wide scan was first executed to examine the overall status of the elements. Raman spectra was measured on a Witec alpha300 Apyron confocal microscope, using a 532-nm excitation source (coherent compass sapphire laser) at a power under 10 mW. The CPO index is defined as follows (*39*)

$$CPO_{hlk/h'l'k'} = \frac{(I_{hlk}/I_{h'l'k'})_M - (I_{hlk}/I_{h'l'k'})_P}{(I_{hlk}/I_{h'l'k'})_P} \quad (5)$$

where I_{hlk} and $I_{h'l'k'}$ are the integrated intensities of the reference and comparison orientation, M and P are the membrane of test and the randomly orientated powder of the membrane material. If the CPO index is ⩾1, then the crystals in the membrane have a preferred (hlk) orientation; if CPO = 0 ~ 1, then the preferred orientation is nominal. In contrast, if CPO is negative, then the membrane crystals even prefer (h′l′k′) orientation (*22*, *40*).

MD simulation

Models

The force field parameters of C_2H_4 and C_2H_6 were obtained from ATB (*41*, *42*).The Lennard-Jones parameters of ZIF-8 were taken from previous work (*43*). The GROMACS 4.67 package was applied to the MD simulations, and the GROMOS96 force fields were used for the grapheme layer (*44*–*48*).

Simulations of separation of C_2H_4 and C_2H_6 along <100> direction

To study the selective penetration of C_2H_4 and C_2H_6 in ZIF-8 membranes, one ZIF-8 cell was placed in a 6.7648 nm by 6.7648 nm by 20.7648 nm simulation box. 500 C_2H_4 and 500 C_2H_6 were put above ZIF-8 cell randomly. One graphene layer was inserted into the bottom of simulation box to collect the penetrated C_2H_4 and C_2H_6 molecules. To observe the selective penetrated behavior at the nanometer scale and the nanosecond scale, the downward ultraforce was applied on the C_2H_4 and C_2H_6 molecules, with the acceleration of 6.75 nm ps^{-2} for C_2H_4 and 6.3 nm ps^{-2} for C_2H_6 molecules after preequilibration. To calculate the diffusion coefficient for C_2H_4 and C_2H_6 molecules during the selective penetration process, the grapheme layer was removed; in this case, the C_2H_4 and C_2H_6 molecules can undergo the loop of penetration without a collective layer. The periodical boundary condition was applied for all the simulation systems. The cutoff distance for short-range nonbonded interactions was chosen to be 12 Å, and long-range electrostatic and V-rescale bath coupling scheme were used (*49*, *50*).The NVT Ensemble were applied, and the simulations were run over 1000 ps in steps of 0.1 fs. The pictures of simulation results were created by VMD (*51*).

SUPPLEMENTARY MATERIALS

Supplementary material for this article is available at https://science.org/doi/10.1126/sciadv.abm6741

REFERENCES AND NOTES

1. M. Safaei, M. M. Foroughi, N. Ebrahimpoor, S. Jahani, A. Omidi, M. Khatami, A review on metal-organic frameworks: Synthesis and applications. *TrAC Trends Anal. Chem.* **118**, 401–425 (2019).
2. M. R. Abdul Hamid, Y. Qian, R. Wei, Z. Li, Y. Pan, Z. Lai, H.-K. Jeong, Polycrystalline metal-organic framework (MOF) membranes for molecular separations: Engineering prospects and challenges. *J. Membr. Sci.* **640**, 119802 (2021).

3. Z. Lai, G. Bonilla, I. Diaz, J. G. Nery, K. Sujaoti, M. A. Amat, E. Kokkoli, O. Terasaki, R. W. Thompson, M. Tsapatsis, D. G. Vlachos, Microstructural optimization of a zeolite membrane for organic vapor separation. *Science* **300**, 456–460 (2003).
4. Y. Sun, Y. Liu, J. Caro, X. Guo, C. Song, Y. Liu, In-plane epitaxial growth of highly *c*-oriented NH_2-MIL-125(Ti) membranes with superior $H2/CO_2$ selectivity. *Angew. Chem. Int. Ed.* **57**, 16088–16093 (2018).
5. Y. Liu, Y. Ban, W. Yang, Microstructural engineering and architectural design of metal–organic framework membranes. *Adv. Mater.* **29**, 1606949 (2017).
6. M. A. Snyder, M. Tsapatsis, Hierarchical nanomanufacturing: From shaped zeolite nanoparticles to high-performance separation membranes. *Angew. Chem. Int. Ed.* **46**, 7560–7573 (2007).
7. Y. Pan, T. Li, G. Lestari, Z. Lai, Effective separation of propylene/propane binary mixtures by ZIF-8 membranes. *J. Membr. Sci.* **390**, 93–98 (2012).
8. R. Wei, H. Y. Chi, X. Li, D. Lu, Y. Wan, C. W. Yang, Z. Lai, Aqueously cathodic deposition of ZIF-8 membranes for superior propylene/propane separation. *Adv. Funct. Mater.* **30**, 1907089 (2020).
9. A. J. Brown, N. A. Brunelli, K. Eum, F. Rashidi, J. R. Johnson, W. J. Koros, C. W. Jones, S. Nair, Interfacial microfluidic processing of metal-organic framework hollow fiber membranes. *Science* **345**, 72–75 (2014).
10. A. Knebel, B. Geppert, K. Volgmann, D. I. Kolokolov, A. G. Stepanov, J. Twiefel, P. Heitjans, D. Volkmer, J. Caro, Defibrillation of soft porous metal-organic frameworks with electric fields. *Science* **358**, 347–351 (2017).
11. C. Zhang, R. P. Lively, K. Zhang, J. R. Johnson, O. Karvan, W. J. Koros, Unexpected molecular sieving properties of zeolitic imidazolate framework-8. *J. Phys. Chem. Lett.* **3**, 2130–2134 (2012).
12. B. Zheng, Y. Pan, Z. Lai, K.-W. Huang, Molecular dynamics simulations on gate opening in ZIF-8: Identification of factors for ethane and propane separation. *Langmuir* **29**, 8865–8872 (2013).
13. C. L. Hobday, C. H. Woodall, M. J. Lennox, M. Frost, K. Kamenev, T. Düren, C. A. Morrison, S. A. Moggach, Understanding the adsorption process in ZIF-8 using high pressure crystallography and computational modelling. *Nat. Commun.* **9**, 1429 (2018).
14. M. Fischer, R. G. Bell, Interaction of hydrogen and carbon dioxide with sod-type zeolitic imidazolate frameworks: A periodic DFT-D study. *CrstEngComm* **16**, 1934–1949 (2014).
15. Y. Liu, G. Zeng, Y. Pan, Z. Lai, Synthesis of highly c-oriented ZIF-69 membranes by secondary growth and their gas permeation properties. *J. Membr. Sci.* **379**, 46–51 (2011).
16. Y. Yoo, Z. Lai, H.-K. Jeong, Fabrication of MOF-5 membranes using microwave-induced rapid seeding and solvothermal secondary growth. *Microp. Mesop. Mater.* **123**, 100–106 (2009).
17. Y. Sun, C. Song, X. Guo, Y. Liu, Concurrent manipulation of out-of-plane and regional in-plane orientations of NH2-UiO-66 membranes with significantly reduced anisotropic grain boundary and superior $H2/CO_2$ separation performance. *ACS Appl. Mater. Interfaces* **12**, 4494–4500 (2020).
18. J. Yan, Y. Sun, T. Ji, L. Liu, M. Zhang, Y. Liu, Cooperative defect tailoring: A promising protocol for exceeding performance limits of state-of-the-art MOF membranes. *J. Membr. Sci.* **635**, 119515 (2021).
19. A. Van der Drift, Evolutionary selection, a principle governing growth orientation in vapour-deposited layers. *Philips Res. Rep.* **22**, 267–288 (1967).
20. A.-J. Bons, P. D. Bons, The development of oblique preferred orientations in zeolite films and membranes. *Microp. Mesop. Mater.* **62**, 9–16 (2003).
21. S. Friebe, B. Geppert, F. Steinbach, J. R. Caro, Metal–organic framework UiO-66 layer: A highly oriented membrane with good selectivity and hydrogen permeance. *ACS Appl. Mater. Interfaces* **9**, 12878–12885 (2017).
22. H. Bux, A. Feldhoff, J. Cravillon, M. Wiebcke, Y.-S. Li, J. Caro, Oriented zeolitic imidazolate framework-8 membrane with sharp H_2/C_3H_8 molecular sieve separation. *Chem. Mater.* **23**, 2262–2269 (2011).
23. O. Shekhah, H. Wang, S. Kowarik, F. Schreiber, M. Paulus, M. Tolan, C. Sternemann, F. Evers, D. Zacher, R. A. Fischer, C. Wöll, Step-by-step route for the synthesis of metal–organic frameworks. *J. Am. Chem. Soc.* **129**, 15118–15119 (2007).
24. O. Shekhah, R. Swaidan, Y. Belmabkhout, M. Du Plessis, T. Jacobs, L. J. Barbour, I. Pinnau, M. Eddaoudi, The liquid phase epitaxy approach for the successful construction of ultra-thin and defect-free ZIF-8 membranes: Pure and mixed gas transport study. *Chem. Commun.* **50**, 2089–2092 (2014).
25. E. P. Valadez Sánchez, H. Gliemann, K. Haas-Santo, C. Wöll, R. Dittmeyer, ZIF-8 SURMOF membranes synthesized by Au-assisted liquid phase epitaxy for application in gas separation. *Chem. Ing. Tech.* **88**, 1798–1805 (2016).
26. Y. Geng, T. Takatani, E. G. Hohenstein, C. D. Sherrill, Accurately characterizing the π–π interaction energies of indole–benzene complexes. *J. Phys. Chem. A* **114**, 3576–3582 (2010).
27. S. M. Brülls, V. Cantatore, Z. Wang, P. L. Tam, P. Malmberg, J. Stubbe, B. Sarkar, I. Panas, J. Mårtensson, S. Eigler, Evidence for electron transfer between graphene and non-covalently bound π-systems. *Chem. A Eur. J.* **26**, 6694–6702 (2020).
28. Y. Pan, Y. Liu, G. Zeng, L. Zhao, Z. Lai, Rapid synthesis of zeolitic imidazolate framework-8 (ZIF-8) nanocrystals in an aqueous system. *Chem. Commun.* **47**, 2071–2073 (2011).
29. P. Y. Moh, "Crystal growth of the metal-organic framework ZIF-8", thesis, University of Manchester (2012).
30. S. Lee, Y. Lei, D. Wang, C. Li, J. Cheng, J. Wang, W. Meng, M. Liu, The study of zeolitic imidazolate framework (ZIF-8) doped polyvinyl alcohol/starch/methyl cellulose blend film. *Polymers* **11**, 1986 (2019).
31. D. Liu, X. Ma, H. Xi, Y. S. Lin, Gas transport properties and propylene/propane separation characteristics of ZIF-8 membranes. *J. Membr. Sci.* **451**, 85–93 (2014).
32. J.-H. Chen, W.-S. Luo, Flexural properties and fracture behavior of nanoporous alumina film by three-point bending test. *Micromachines* **8**, 206 (2017).
33. G. Yamamoto, T. Hashida, Carbon nanotube reinforced alumina composite materials, in *Composites and Their Properties*, N. Hu, Ed. (IntechOpen, 2012).
34. M. Rungta, C. Zhang, W. J. Koros, L. Xu, Membrane-based ethylene/ethane separation: The upper bound and beyond. *AIChE J.* **59**, 3475–3489 (2013).
35. S. M. Lai, L. T. Y. Au, K. L. Yeung, Influence of the synthesis conditions and growth environment on MFI zeolite film orientation. *Microp. Mesop. Mater.* **54**, 63–77 (2002).
36. P. Cubillas, M. W. Anderson, M. P. Attfield, Crystal growth mechanisms and morphological control of the prototypical metal–organic framework MOF-5 revealed by atomic force microscopy. *Chem. A Eur. J.* **18**, 15406–15415 (2012).
37. P. Y. Moh, P. Cubillas, M. W. Anderson, M. P. Attfield, Revelation of the molecular assembly of the nanoporous metal organic framework ZIF-8. *J. Am. Chem. Soc.* **133**, 13304–13307 (2011).
38. Z. Zhou, D. Guo, D. B. Shinde, L. Cao, Z. Li, X. Li, D. Lu, Z. Lai, Precise sub-angstrom ion separation using conjugated microporous polymer membranes. *ACS Nano* **15**, 11970–11980 (2021).
39. J. P. Verduijn, A. J. Bons, M. H. Anthonis, L. H. Czarnetzki, *Int. Pat. Appl. PCT* WO 96/01683 (1996).
40. L. Diestel, X. L. Liu, Y. S. Li, W. S. Yang, J. Caro, Comparative permeation studies on three supported membranes: Pure ZIF-8, pure polymethylphenylsiloxane, and mixed matrix membranes. *Microp. Mesop. Mater.* **189**, 210–215 (2014).
41. M. Stroet, B. Caron, K. M. Visscher, D. P. Geerke, A. K. Malde, A. E. Mark, Automated topology builder version 3.0: Prediction of solvation free enthalpies in water and hexane. *J. Chem. Theory Comput.* **14**, 5834–5845 (2018).
42. A. K. Malde, L. Zuo, M. Breeze, M. Stroet, D. Poger, P. C. Nair, C. Oostenbrink, A. E. Mark, An Automated Force Field Topology Builder (ATB) and repository: Version 1.0. *J. Chem. Theory Comput.* **7**, 4026–4037 (2011).
43. B. Zheng, M. Sant, P. Demontis, G. B. Suffritti, Force field for molecular dynamics computations in flexible ZIF-8 framework. *J. Phys. Chem. C* **116**, 933–938 (2012).
44. W. F. van Gunsteren, S. R. Billeter, A. A. Eising, P. H. Hünenberger, P. Krüger, A. E. Mark, W. R. P. Scott, I. G. Tironi, *Biomolecular Simulation: The GROMOS96 Manual and User Guide* (Hochschulverlag AG an der ETH Zürich, Zürich, Switzerland, 1996).
45. B. Hess, C. Kutzner, D. van der Spoel, E. Lindahl, GROMACS 4: Algorithms for highly efficient, load-balanced, and scalable molecular simulation. *J. Chem. Theory Comput.* **4**, 435–447 (2008).
46. D. Van Der Spoel, E. Lindahl, B. Hess, G. Groenhof, A. E. Mark, H. J. C. Berendsen, GROMACS: Fast, flexible, and free. *J. Comput. Chem.* **26**, 1701–1718 (2005).
47. E. Lindahl, B. Hess, D. van der Spoel, GROMACS 3.0: A package for molecular simulation and trajectory analysis. *Mol. Mod. Annu.* **7**, 306–317 (2001).
48. C. Oostenbrink, A. Villa, A. E. Mark, W. F. Van Gunsteren, A biomolecular force field based on the free enthalpy of hydration and solvation: The GROMOS force-field parameter sets 53A5 and 53A6. *J. Comput. Chem.* **25**, 1656–1676 (2004).
49. H. J. C. Berendsen, J. P. M. Postma, W. F. Vangunsteren, A. Dinola, J. R. Haak, Molecular-dynamics with coupling to an external bath. *J. Chem. Phys.* **81**, 3684–3690 (1984).
50. G. Bussi, D. Donadio, M. Parrinello, Canonical sampling through velocity rescaling. *J. Chem. Phys.* **126**, 014101 (2007).
51. W. Humphrey, A. Dalke, K. Schulten, VMD: Visual molecular dynamics. *J. Mol. Graph.* **14**, 33–38 (1996).
52. X. Yang, Z. Wen, Z. Wu, X. Luo, Synthesis of ZnO/ZIF-8 hybrid photocatalysts derived from ZIF-8 with enhanced photocatalytic activity. *Inorg. Chem. Front.* **5**, 687–693 (2018).
53. M. S. Dresselhaus, A. Jorio, M. Hofmann, G. Dresselhaus, R. Saito, Perspectives on carbon nanotubes and graphene Raman spectroscopy. *Nano Lett.* **10**, 751–758 (2010).
54. A. Jorio, R. Saito, Raman spectroscopy for carbon nanotube applications. *J. Appl. Phys.* **129**, 021102 (2021).
55. G. Xue, Q. Dai, S. Jiang, Chemical reactions of imidazole with metallic silver studied by the use of SERS and XPS techniques. *J. Am. Chem. Soc.* **110**, 2393–2395 (1988).
56. T. I. T. Okpalugo, P. Papakonstantinou, H. Murphy, J. McLaughlin, N. M. D. Brown, High resolution XPS characterization of chemical functionalised MWCNTs and SWCNTs. *Carbon* **43**, 153–161 (2005).

57. A. Theodosiou, B. F. Spencer, J. Counsell, A. N. Jones, An XPS/UPS study of the surface/near-surface bonding in nuclear grade graphites: A comparison of monatomic and cluster depth-profiling techniques. *Appl. Surf. Sci.* **508**, 144764 (2020).
58. H. K. Jeong, E. Echeverria, P. Chakraborti, H. T. Le, P. A. Dowben, Electronic structure of cyclodextrin–carbon nanotube composite films. *RSC Adv.* **7**, 10968–10972 (2017).

Acknowledgments
Funding: The research was supported by King Abdullah University of Science and Technology URF/1/3769-01. **Author contributions:** Conceptualization: R.W., X. Liu., Z.Z., and Z. Lai. Methodology: R.W., X. Liu., Z.Z., and Z. Lai. Investigation: R.W., X. Liu., Z.Z., C.C., Y.Y., Z. Li., X. Li., X.D., D.L., and Y.H. Validation: R.W. and X. Liu. Visualization: R.W. and X. Liu. Writing (original draft): R.W. Writing (review and editing): R.W., X. Liu., and Z. Lai. Supervision: Z. Lai. **Competing interests:** The authors declare that they have no competing interests. **Data and materials availability:** All data necessary to support the conclusions in the paper are present in the paper and/or the Supplementary Materials.

Submitted 15 October 2021
Accepted 23 December 2021
Published 16 February 2022
10.1126/sciadv.abm6741